Symmetry analysis of the photoelectron continuum in two-photon XUV + IR ionization

A. S. Kheifets ◉*

Research School of Physics, The Australian National University, Canberra Australian Capital Territory 2601, Australia

The photoelectron momentum distribution (PMD) in two-photon XUV-IR ionization of Ne is studied theoretically by numerical solution of the time-dependent Schrödinger equation and within the analytical soft photon approximation. The symmetry of the PMD, projected on the plane encompassing the joint XUV-IR linear polarization axis, reveals the angular momentum composition of the photoelectron wave packet. This composition, in turn, allows to examine the validity of the angular momentum propensity rules which govern the bound-continuum and continuum-continuum photon driven transitions. The Fano propensity rule for bound-continuum transitions that favors an increase in the angular momentum is confirmed. However, its extension to continuum-continuum transitions suggested by Busto *et al.* [Phys. Rev. Lett. **123**, 133201 (2019)] is less straightforward. In addition, we break the time-reversal symmetry of the XUV field by combining the odd and even multiples of the fundamental frequency. By doing so, we change the time and angular structure of the photoelectron continuum.

I. INTRODUCTION

A high-precision synchronization of the XUV pump and IR probe laser pulses allows to resolve atomic and molecular ionization on the attosecond timescale. Isolated XUV pulses are used to drive the attosecond streak camera [1]. Attosecond pulse trains (APTs) are utilized in the technique of reconstruction of attosecond bursts by beating of two-photon transitions (RABBITT) [2–4]. RABBITT exploits a two-path interference in which primary XUV ionization is augmented by an IR photon absorption or emission, both processes leading to the identical final state. This state reveals itself in the photoelectron spectrum as a sideband (SB) of an even-order SB_{2q} which is sandwiched between the adjacent primary harmonic (H) peaks H_{2q-1} and H_{2q+1}. As the time-separation τ between the XUV and the IR pulses varies, the magnitude of the sideband oscillates with the twice the fundamental photon frequency,

$$S_{2q}(\tau) = A + B \cos[2\omega\tau - C]. \tag{1}$$

Here A and B are the magnitude parameters, whereas C is the RABBITT phase. These parameters, which factorize the τ dependence, are sensitive to the photoelectron emission angle relative to the joint polarization axis of the XUV and IR fields which are both linearly polarized. The angular dependence of the RABBITT parameters have been determined experimentally [5–7] and studied theoretically [8,9]. Initially [5], the measurements were focused on the RABBITT phase that allowed to determine the anisotropic time delay of the two-color atomic ionization $\tau_a = C/(2\omega)$ and its individual XUV and IR constituents. These constituents were attributed, respectively, to the Wigner time-delay τ_W and the continuum-continuum

correction τ_{cc} [10]. In subsequent experiments [6,7], the RABBITT magnitude parameters were also analyzed in terms of the angular anisotropy β parameters. In a general case, two-photon ionization requires an introduction of a pair of β_2, β_4 parameters [11]. In a weak-field regime when the soft photon approximation applies [12], this pair is reduced to a single β parameter which can be compared directly with the values known from earlier synchrotron measurements [9,13].

The lowest sideband is distinct in RABBITT. One of its adjacent primary harmonic peaks H_{2q-1} submerges below the ionization threshold and is missing in the photoelectron spectrum. Instead, XUV ionization aided by IR absorption proceeds via an intermediate discrete atomic excitation. Such an underthreshold (uRABBITT) process was observed experimentally in He [14] and Ne [15]. The latter Ne measurement was angular resolved. Rather than factorizing the RABBITT signal in the form of Eq. (1), a direct imaging of the PMD was performed in Ref. [15] by projecting it onto the plane containing the joint polarization axis of the XUV and IR laser pulses. Such an imaging revealed a clear f symmetry of the PMD with a strong propensity of the $m = 0$ magnetic projection in the final photoelectron wave packet. Initially, this propensity was attributed to the m-dependent Stark energy shift of the intermediate $3d$ state. Later [16], a more involved explanation was proposed based on the dynamic polarizability of the intermediate $3p$ and $3d$ discrete states. The selective population of the $m = 1$ ionization continuum was also demonstrated by appropriately tuning the driving laser pulse parameters.

The population of the f-ionization continuum seems to be natural in two-photon ionization of the np-valence shells of noble gases. In conventional RABBITT, the Fano propensity rule [17] requires the XUV-driven bound-continuum transitions to proceed via an intermediate ϵd state. The subsequent IR absorption also favors an increase in the photoelectron angular momentum [7]. In uRABBITT [18,19], the

*Corresponding author: A.Kheifest@anu.edu.au

bound-bound transitions occur with comparable oscillator strength into intermediate ns and nd states whereas the subsequent IR-driven ionization favors very strongly the final f continuum.

In the present paper, we adopt the technique of the PMD projection and subsequent symmetry analysis of the photoelectron wave packet employed in Refs. [15,16]. We use this technique to analyze the angular momentum composition of the photoelectron continuum in conventional and uRABBITT processes on Ne. Whereas the f symmetry of the uRABBITT photoelectron continuum is confirmed, the angular composition of the conventional RABBITT continuum is generally more complex. We also derive and analyze the angular dependence of the RABBITT parameters in Eq. (1). We examine validity of the soft photon approximation (SPA) and observe its onset at the half the periods of the RABBITT oscillation. This explains the periodic oscillation of the β_2 parameters observed in Ref. [7]. Finally, we admix even harmonics to the APT and make RABBITT a three-path interference process. By doing so, we change profoundly both the time and the angular structure of the photoelectron continuum.

II. THEORETICAL METHODS

A. Numerical techniques

As previously [8,9], we solve numerically the one-electron TDSE for a target atom,[1]

$$i \, \partial \Psi(\boldsymbol{r})/\partial t = [\hat{H}_{\text{atom}} + \hat{H}_{\text{int}}(t)]\Psi(\boldsymbol{r}), \qquad (2)$$

where the radial part of the atomic Hamiltonian,

$$\hat{H}_{\text{atom}}(r) = -\frac{1}{2}\frac{d^2}{dr^2} + \frac{l(l+1)}{2r^2} + V(r) \qquad (3)$$

contains an effective one-electron potential $V(r)$. The said potential is obtained by localization of the nonlocal Hartree-Fock potential using a numerical recipe suggested in Ref. [20]. The accuracy of such a LHF potential in the present application was tested and confirmed in Ref. [19] by comparing the bound-state energies of Ne with the reference data base [21]. The Hamiltonian $\hat{H}_{\text{int}}(t)$ describes interaction with the external field and is written in the velocity gauge,

$$\hat{H}_{\text{int}}(t) = \boldsymbol{A}(t) \cdot \hat{\boldsymbol{p}}, \quad \boldsymbol{A}(t) = -\int_0^t \boldsymbol{E}(t') \, dt'. \qquad (4)$$

The driving field is composed of the linearly polarized XUV and IR pulses. The XUV field is modeled by an APT with the vector potential,

$$\begin{aligned} A_x(t) = \sum_{n=-20}^{20} A_n \exp\left(-2 \ln 2 \frac{(t - nT/2)^2}{\tau_x^2}\right) \\ \times \cos[\omega_x(t - nT/2) + \Phi_n], \\ \Phi_n = [1 - (-1)^n]\frac{\pi}{2}, \end{aligned} \qquad (5)$$

where

$$A_n = A_0 \exp\left(-2 \ln 2 \frac{(nT/2)^2}{\tau_T^2}\right). \qquad (6)$$

Here A_0 is the vector potential peak value, and $T = 2\pi/\omega$ is the period of the IR field. The phase Φ_n makes the vector potential an odd function relative to the time inversion about its center. Hence, the XUV spectrum contains only the odd harmonics of the fundamental frequency ω. In the present application, the APT is centered at $\omega_x = 15\omega$, and its spectral width is reduced to $\Gamma = 0.1$ eV by increasing the number of pulselets to $N = 41$ with $\tau_T = 18$ fs and $\tau_x = 30$ as. The fundamental frequency is set to $\omega = 1.54$ eV ($\lambda = 805$ nm). This choice corresponds to the maximum overlap of the submerged harmonic H13 with the discrete $3d$ state of Ne calculated in the LHF potential (see Fig. 5(c) of [19]).

The vector potential of the IR pulse is represented by the cosine-squared envelope,

$$A(t) = A_0 \cos^2\left(\frac{\pi(t - \tau)}{2\tau_{\text{IR}}}\right) \cos[\omega(t - \tau)], \qquad (7)$$

with $\tau_{\text{IR}} = 15$ fs. Intensities of the XUV and IR pulses were maintained in the 0.01 TW $= 1 \times 10^{10}$ W/cm^2 range. This is significantly lower than the 1 TW/cm^2 range employed in Refs. [15,16]. The present choice was motivated by several factors. First, at larger intensities in the 1 TW/cm^2 range, the prime harmonic peaks become affected by the IR field and their magnitude starts to oscillate with a varying XUV-IR delay τ. In the present paper, we use these peaks as a stable reference and would want to avoid this oscillation. Second, we would like to compare our numerical results with predictions of the lowest-order perturbation theory described in the next section. The lower-field intensity regime suits this purpose. In addition, in this regime, the numerical results become least sensitive to selection of the specific field parameters in Eqs. (5) and (7).

The solution of the time-dependent Schrödinger equation (TDSE) (2) was found by using the spherical-coordinate implicit derivatives (SCID) computer code [22]. The PMD was obtained with the time-dependent surface flux method [23,24]. In the present application, the Volkov Hamiltonian was used, and the PMD was obtained by projecting the time-dependent wave function after the end of the propagation on the basis of the plane waves,

$$P(\boldsymbol{k}) = |\langle \varphi_{\boldsymbol{k}}(r)|\Psi_{nlm}(\boldsymbol{r}, t \to \infty)|\rangle|^2. \qquad (8)$$

Here the indices n, l, m denote the initial atomic bound state (the Ne $2p_m$ ground state). The photoelectron momentum $\boldsymbol{k}$ is defined in the Cartesian plane in which the $\hat{z}$ axis is aligned with the joint polarization direction of the XUV and IR pulses. The (x, y) plane is perpendicular to this direction. Because of the rotational symmetry relative to the polarization direction, the orthogonal $\hat{x}$ and $\hat{y}$ axes can be directed arbitrarily on the (x, y) plane.

The photoelectron spectrum is obtained by the angular integration of Eq. (8),

$$P(E) = \int k^2 d\Omega_k \, P(\boldsymbol{k}), \quad E = k^2/2. \qquad (9)$$

---

[1] Here and throughout, we use the atomic units (a.u.) by setting $e = m = \hbar = 1$.

Projection on the $k_y = 0$ plane $P(k_x, k_z)$ serves to determine the angular profile of a given sideband,

$$P_{2q}(\theta) = \int k^2 dk \, P(k_x, k_z), \quad \theta = \tan^{-1}(k_z/k_x)$$

$$E_{2q} - \Gamma/2 < k_x^2 + k_z^2 < E_{2q} + \Gamma/2. \tag{10}$$

Here the sideband is positioned at $E_{2q} = 2q\omega - I_p$, and we neglect the ponderomotive term in the energy conservation because of the low-field intensity. The angular momentum projection m and the XUV-IR delay τ are implicit in Eqs. (9) and (10) but not shown for brevity of notations. Because of the rotational symmetry with respect to the polarization axis $\hat{z}$ and the reflection symmetry relative to the $k_z = 0$ equatorial plane, $P(\theta)$ is uniquely determined on the $\theta \in [0, \pi/2]$ interval. The polarization direction corresponds to $\theta = 0$.

B. Lowest-order perturbation theory

The simplest description of the RABBITT process is provided by the lowest-order perturbation theory (LOPT) with respect to the photon-atom interaction [10,25]. In this approach, the spectral strength of a given sideband can be expressed as

$$S_{2q}(\tau) = |\mathcal{M}_k^{(-)} e^{-i\omega\tau} + \mathcal{M}_k^{(+)} e^{+i\omega\tau}|^2, \tag{11}$$

where $\mathcal{M}_k^{(\pm)}$ are complex amplitudes for the angle-resolved photoelectron produced by adding or subtracting an IR photon, respectively. Accordingly, the RABBITT parameters A, B, and C entering Eq. (1) can be expressed as

$$A = |\mathcal{M}_k^{(-)}|^2 + |\mathcal{M}_k^{(+)}|^2,$$
$$B = 2|\mathcal{M}_k^{(-)} \mathcal{M}_k^{(+)}|$$
$$C = \arg[\mathcal{M}_k^{(-)} \mathcal{M}_k^{*(+)}] = 2\omega\tau_a. \tag{12}$$

By adopting the SPA [12] one can write [9]

$$A, B \propto [1 + \beta P_2(\cos\theta)] \cos^2\theta. \tag{13}$$

A more general parametrization for the angular dependence of the SB magnitude reads [11]

$$P_{2q}(\theta) \propto 1 + \beta_2 P_2(\cos\theta) + \beta_4 P_4(\cos\theta). \tag{14}$$

However, in the SPA, the two sets of the angular anisotropy parameters β_2, β_4 in Eq. (14) can be expressed via the single set β [9]. By expanding Eq. (13) over the Legendre polynomials, one arrives at the following expressions:

$$\beta_2 = \frac{70 + 55\beta}{35 + 14\beta}, \quad \beta_4 = \frac{36\beta}{35 + 14\beta}, \quad \beta_2 - \frac{3}{4}\beta_4 = 2. \tag{15}$$

The last identity of Eq. (15) connects the β_2, β_4 parameters and makes one of them redundant. It also allows expressing the one-photon anisotropy parameter as

$$\beta = \frac{35\beta_2 - 70}{55 - 14\beta_2}. \tag{16}$$

This conventional β parameter can also be extracted from the angular dependence of the primary harmonic peaks,

$$P_{2q\pm1}(\theta) \propto 1 + \beta P_2(\cos\theta). \tag{17}$$

The angular dependence of the amplitudes $\mathcal{M}_k^{\pm}$ can be deduced from the following LOPT expression [10]:

$$\mathcal{M}_k^{\pm} \propto \sum_{\lambda=l_i\pm1} \sum_{L=\lambda\pm1} (-i)^L e^{i\eta_L} Y_{LM}(\hat{k})$$

$$\times \left\{ \sum_{E_v < 0} \frac{\langle kL\|r\|E_n\lambda\rangle\langle E_n\lambda\|r\|l_i n_i\rangle}{E_i + \Omega^\pm - E_n - i\gamma} \right.$$

$$\left. + \int_0^\infty d^3\kappa \frac{\langle kL\|r\|\kappa\lambda\rangle\langle\kappa\lambda\|r\|l_i n_i\rangle}{E_i + \Omega^\pm - \kappa^2/2 - i\gamma} \right\}. \tag{18}$$

For the conventional and uRABBITT processes, it is, respectively, the integral over the continuum and the discrete sum in the right-hand side of Eq. (18) that make the dominant contribution. In the above equation, $\langle n_i l_i|$, $\langle\kappa\lambda|$, and $\langle kL|$ are the initial, intermediate, and final states defined by their linear and angular momenta, the latter are determined by the angular momentum coupling rule. The XUV photon energy is $\Omega^\pm = (2q \pm 1)\omega$ and $i\gamma$ denotes the pole bypass on the complex energy plane.

The reduced dipole matrix elements entering Eq. (18) encode the Fano propensity rule as

$$|\langle\kappa(l_i + 1)\|r\|l_i n_i\rangle| \gg |\langle\kappa(l_i - 1)\|r\|l_i n_i\rangle|. \tag{19}$$

The explanation of the angular momentum propensity in the continuum-continuum transition $\lambda \to L$ is more subtle [7]. It rests on the centrifugal energy term in the atomic Hamiltonian (3) which serves to take the final local momentum $k(r) = \sqrt{2[E - V(r)]}$ closer to that in the intermediate-state $\kappa(r)$. Thus, in the case of absorption $(+)$ or emission $(-)$ of a photon, increasing $\lambda \to \lambda + 1$ or decreasing $\lambda \to \lambda - 1$ angular momentum is favored. To express these conditions, we adopt the notations of Busto *et al.* [7] and introduce the two-photon-reduced matrix elements,

$$M_{\lambda L}^{(\pm)} = \int_0^\infty d^3\kappa \frac{\langle kL\|r\|\kappa\lambda\rangle\langle\kappa\lambda\|r\|l_i n_i\rangle}{E_i + \Omega^\pm - \kappa^2/2 - i\gamma}, \tag{20}$$

Busto *et al.* [7] noted that the following inequalities are satisfied:

$$\frac{|M_{\lambda\lambda+1}^{(+)}|}{|M_{\lambda\lambda-1}^{(+)}|} > 1, \quad \frac{|M_{\lambda\lambda+1}^{(+)}|}{|M_{\lambda\lambda+1}^{(-)}|} > 1, \quad \frac{|M_{\lambda\lambda-1}^{(-)}|}{|M_{\lambda\lambda-1}^{(+)}|} > 1. \tag{21}$$

This first inequality means that the angular momentum increase is favored in the photon absorption process. The two other inequalities indicate that the absorption of the photon is favored over its emission when the photoelectron angular momentum is increased and vice versa. As the absorption and emission processes are entangled in the RABBITT process, the last two inequalities in Eq. (21) cannot be tested within the TDSE formalism. To test whether the increase of the photoelectron angular momentum is actually favored in RABBITT, we may analyze the deduced ratio,

$$\frac{|M_{\lambda\lambda+1}^{(+)}|}{|M_{\lambda\lambda-1}^{(-)}|} = \frac{|M_{\lambda\lambda+1}^{(+)}|}{|M_{\lambda\lambda-1}^{(+)}|} \left[\frac{|M_{\lambda\lambda-1}^{(-)}|}{|M_{\lambda\lambda-1}^{(+)}|}\right]^{-1}. \tag{22}$$

From the numerical values given by Busto *et al.* we see that this ratio is indeed greater than one for Ne in the extended photoelectron energy range.
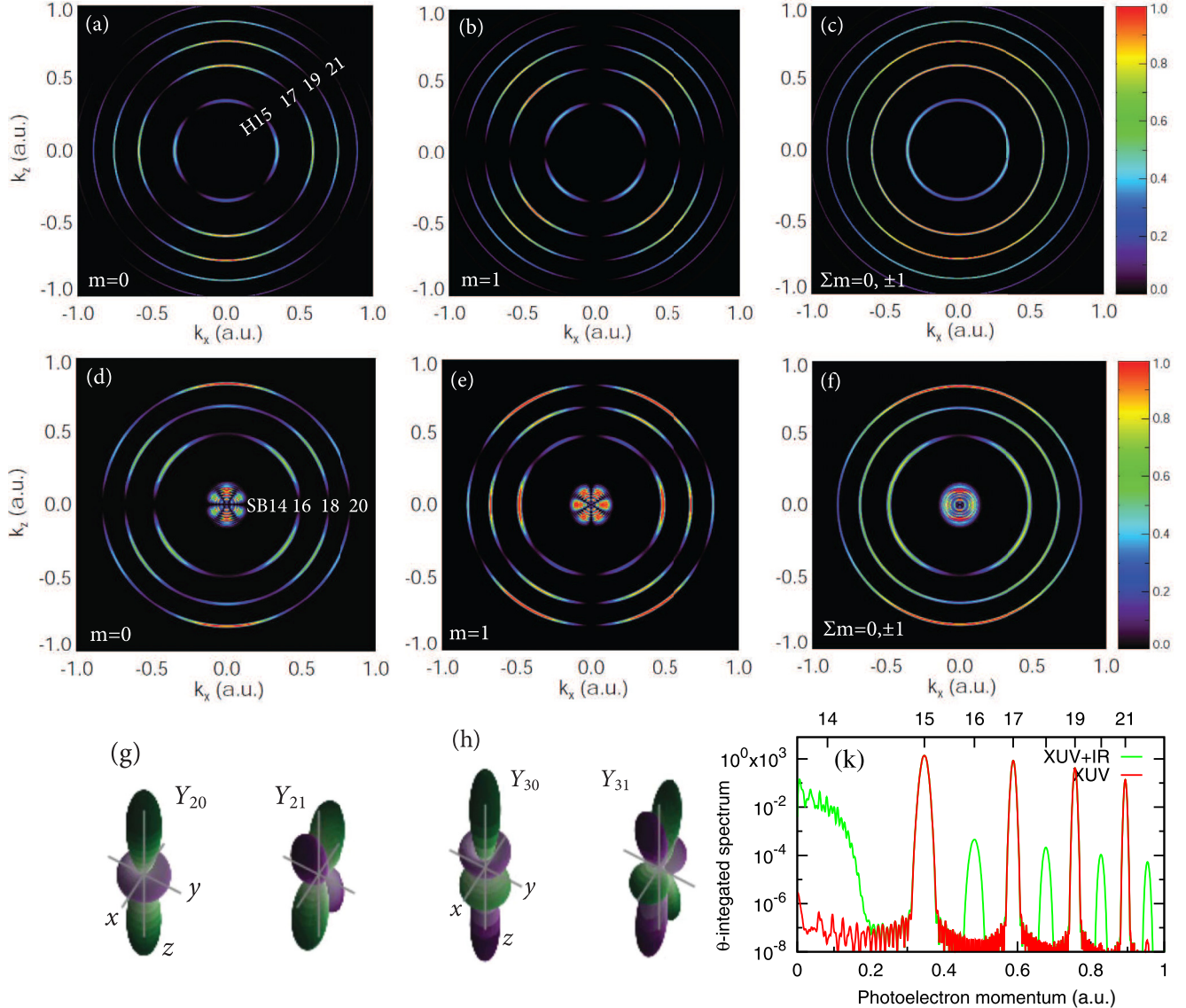
FIG. 1. PMD of Ne $P(k_x, k_z)$ projected on the $p_y = 0$ plane. Top row: the prime harmonic peaks H15–21 corresponding to the initial $2p_m$ state prepared with (a) $m = 0$, (b) $m = 1$, and (c) the incoherent sum $\Sigma m = 0, \pm 1$. Middle row: The same for the sidebands (d) with $m = 0$, (e) $m = 1$, and (f) $\Sigma m = 0, \pm 1$. The bottom row: panels (g) and (h) visualize the spherical harmonics Y_{2m} and Y_{3m} which reflect the symmetry of the primary harmonic peaks and the sidebands, respectively. Panel (k) displays the angular integrated photoelectron spectrum showing the primary harmonic peaks (red, XUV only) and sidebands (green, XUV+IR).

III. NUMERICAL RESULTS AND DISCUSSION

A. Odd XUV harmonic spectrum

The PMD $P(k_x, k_z)$ projected on the $k_y = 0$ plane is displayed in Fig. 1. The top row of panels exhibits the projection of the main harmonic peaks H15–21. The three separate cases are considered with the $2p_m$ initial state of Ne being prepared with (a) $m = 0$, (b) $m = 1$, (c) and the PMD taken as an incoherenet sum $\Sigma m = 0, \pm 1$. The latter case corresponds to an unpolarized target atom. As seen from the photoelectron spectrum $P(E)$ displayed in panel (k), the sidebands are significantly lower in magnitude in comparison to the primary harmonic peaks and are normally hardly discernible in PMD. To highlight the sidebands, we subtract the single-photon XUV spectrum from the two-photon XUV + IR one. Both spectra contain the same harmonic peaks which cancel out in

the difference spectrum. In this way, the sidebands become clearly discernible as displayed in panels (d)–(f).

The Fano propensity rule for the bound-continuum transitions driven by XUV absorption requires the d-wave symmetry for the primary harmonic peaks. The Y_{2m} symmetry, which can be inferred from the three-dimensional images of panel (g), is indeed exhibited very clearly in panels (a) and (b). This can be seen from the peaks and nodes in the equatorial $k_z = 0$ plane and the polarization $\hat{z}$ direction. The alternative s-wave population, that would have filled the nodes, is manifestly absent. The IR-driven continuum-continuum transitions from the intermediate d wave would lead to the p- and f-wave population in the final continuum. The Fano propensity rule would have favored the f wave. The f symmetry, visualized by Y_{3m} in panel (h), can indeed be seen for the sidebands, especially SB14. This confirms the observation of Refs. [15,16].

TABLE I. Angular momentum decomposition of the two-photon continuum in sidebands SB14–20.

| SB | $|Y_{30} + ae^{i\phi_{13}}Y_{10}|^2, \quad m = 0$ | | | | $|Y_{31} + ae^{i\phi_{13}}Y_{11}|^2, \quad m = 1$ | | | |
| | $\tau = 0$ | | $\tau = 20$ a.u. | | $\tau = 0$ | | $\tau = 20$ a.u. | |
$2q$	a	ϕ	a	ϕ	a	ϕ	a	ϕ
14	0.53	2.42	0.25	1.79	0.28	0.98	0.30	2.39
16	1.80	2.96	0.66	1.44	0.71	0.54	0.60	2.66
18	1.01	2.61	0.79	1.03	0.28	0.89	0.57	2.86
20	0.55	1.99	0.87	0.83	0.14	2.29	0.56	2.95

However, the $m = 0$ propensity is not so obvious in our case for the unpolarized target atom. We also note that the p wave would have displayed the same peaks and nodes in the equatorial plane and the polarization direction. Thus, the admixture of the p wave to the f wave would not have been so obvious for sidebands other than SB14.

To break down the angular momentum composition of the sidebands, we conduct a more detailed analysis of the angular profiles $P_{2q}(\theta)$ as defined by Eq. (10) and illustrated in Fig. 2. The four panels of Fig. 2 correspond to the two angular momentum projections $m = 0, 1$ of the initial $2p_m$ state and the two values of the XUV-IR delay $\tau = 0$ and 20 a.u. For visual convenience, all the angular profiles are normalized to unity. The two cases of $m = 0$ (a) and (c) and $m = 1$ (b) and (d) differ manifestly as the angular positions of the peaks and the nodes at 0 and 90° are swapped. The only exception is the $m = 1$ case at $\tau = 20$ a.u. where the angular maximum at 90°, displayed boldly at $\tau = 0$, is strongly suppressed for SB16–20. To see more clearly the angular momentum decomposition of the final two-photon continuum, we infer the angular dependence of the two-photon matrix elements from Eq. (18) and fit the angular profiles of Fig. 2 with the corresponding analytic expression,

$$P_{2q}(\theta) \propto |Y_{3m}(\theta) + ae^{i\phi_{13}}Y_{1m}(\theta)|^2. \tag{23}$$

Here a real coefficient a specifies the fraction of the p wave admixed to the f wave and a complex factor $\exp(i\phi_{13})$ denotes their relative phase shift. These factors are summarized in Table I. If one neglects the atomic potential, the elastic scattering phases η_L depend weakly on L and the phase difference $\phi_{13} \sim \pi$ would come mostly from the kinematic factor $(-i)^L$.

As expected from the images displayed in Fig. 1, the admixture of the p wave to the f wave is smallest for the lowest SB14. This is quite understandable because the SB14 population in the uRABBITT regime is driven by a discrete-continuum transition. For the next SB16, this admixture is rather strong, especially at $\tau = 0$ with the mixing coefficient $a \simeq 1$. For higher SB18–20, the mixing of the p wave is gradually reduced. However, at $\tau = 20$ a.u. such admixture remains noticeable. This observation does not support a straightforward extension of the Fano angular momentum propensity rule [17] to the continuum-continuum transitions.

Figure 2 displays a strong modification of the SB angular profiles with an increase in the XIV-IR delay τ. This modification is particularly drastic in the $m = 1$ case when the equatorial maximum at $\theta = 90°$ and $\tau = 0$ is reduced to a node at $\tau = 20$ a.u. for all the sidebands except SB14. To understand the nature of this modification, we perform the

summation of the angular profiles over the angular momentum projections $\Sigma m = 0, \pm 1$ and apply the angular anisotropy parametrization of Eq. (14).

In Fig. 3, we display the m-summed angular profiles of SB14–20 at the three values of the XIV-IR delay (a) $\tau = 0$, (b) $\tau = 10$ a.u., and (c) $\tau = 20$ a.u.. We recall that at $\lambda \sim 800$ nm the period of the RABBITT oscillation $T_2 = 2\pi/(2\omega) \simeq 55$ a.u. = 1.3 fs. So the case (c) corresponds to $\tau \sim T_2/2$. The τ modification of the angular profiles in Fig. 3 is striking. A broad disparity of the angular dependence between the four sidebands at (a) $\tau = 0$ is gradually reduced to a nearly complete uniformity at (c) $\tau = 20$ a.u.. In the latter case, all the angular profiles display a strong maximum in the polarization direction $\theta = 0$ and a node in the equatorial plane $\theta = \pi/2$. Such a behavior is a signature of the $\cos^2 \theta$ factor present in the SPA expression (13). The only exception from this behavior is the SB14 which displays a minimum instead of a node.

The angular anisotropy β_2, β_4 parameters deduced from the fit with Eq. (14) are summarized in Table II. To follow the trend with an increasing SB order, we expand our analysis to SB14–24. Except for the uRABBITT SB14, other sidebands follow the similar trends. With an increasing SB order and the corresponding photoelectron energy, the β_2 parameter grows steadily approaching the SPA identity $\beta_2 - \frac{3}{4}\beta_4 = 2$. This identity is satisfied particularly accurately at $\tau = 20$ a.u. for SBs of higher order. This allows one to express the conventional β parameter via β_2 using Eq. (16) and to compare it with another set of β values extracted from the angular dependence of the prime harmonic peaks using Eq. (17). This comparison is displayed in Fig. 4 together with the experiment [26] and another time-independent calculation performed within the RPAE [9]. All the four sets of β values agree well between themselves.

The β_2 parameters for various sidebands as functions of the XUV-IR delay τ are plotted in the top panel of Fig. 4. One can observe in this plot a strong congestion of the β_2 values at half periods and their greater divergence at integer number of periods across various sidebands except SB14. Such a behavior was documented in Ar (see Fig. 4 of Ref. [7]). However, no explanation of this phenomenon was offered other than a statement of good agreement between the theory and experiment. In the following, we attribute these oscillations of the β_2 parameters to the onset of the SPA.

To understand this gradual transition towards the SPA, we extract the RABBITT parameters A, B, C from Eq. (1) and plot them as functions of the photoelectron ejection angle θ. These plots are shown in Fig. 5. The raw data points are joined by the similarly colored solid lines which represent the

TABLE II. Angular anisotropy β parameters obtained from the fit of the SB angular profiles with Eq. (14) for various XUV-IR delays τ. The SPA identity (15) $\Sigma_\beta \equiv \beta_2 - \frac{3}{4}\beta_4 = 2$ is tested where sensible.

SB	β_2	β_4	Σ_β	β_2	β_4	Σ_β	β_2	β_4	Σ_β
		$\tau = 0$			$\tau = 10$ a.u.			$\tau = 20$ a.u.	
14	0.15	0.33		0.82	0.17		1.39	0.04	
16	−0.46	−0.47		0.92	−0.44		1.60	−0.26	1.78
18	−0.04	−0.40		1.63	−0.03	1.65	2.03	0.13	1.93
20	1.07	0.06		2.00	0.26	1.80	2.24	0.37	1.96
22	1.88	0.43	1.55	2.23	0.46	1.89	2.36	0.52	1.97
24	2.23	0.60	1.78	2.36	0.59	1.91	2.44	0.62	1.98

analytic fit,

$$A, B = a[1 + \beta_2 P_2(\cos\theta) + \beta_4 P_4(\cos\theta)],$$
$$C = \arg[P_3(\cos\theta)e^{i\phi_3} + bP_1(\cos\theta)e^{i\phi_1}]. \quad (24)$$

Fitting the magnitude parameters with the analogous SPA expression (13) is less accurate, and it breaks near 90° where the coefficients A, B do not vanish, especially for SB14. In the meantime, the phase parameter C stays nearly flat for the most of its angular range with the exception of SB14. The C parameter starts changing with θ when the contributions of the p and f waves become comparable and their respective phase factors ϕ_1, ϕ_3 make their distinct contributions, underpinned by the respective spherical harmonics. In SB14, which is dominated strongly by the f wave, this happens near the kinematic node of $Y_{30}(39.3°)$. In other sidebands, the angular change of phase occurs at significantly larger angles tending towards 90° as the SB order grows.

We invoke this angular behavior of the A, B, C parameters coupled with the τ dependence of Eq. (1) to explain the observed peculiarities of the SB angular profiles. Both magnitude parameters $A \approx B$ for most of their angular range except for the close proximity to 90°. In the same angular range $C \sim \pi$ and, thus,

$$S_{2q}(\tau) \simeq A - B\cos[2\omega\tau] = \begin{cases} A - B, & \tau = 0. \\ A + B, & \tau = T_2/2. \end{cases} \quad (25)$$

The factor $A - B$ at $\tau = 0$ is very sensitive to a small deviation of the A and B parameters from each other because of a minor difference between the absorption and the emission amplitudes $\mathcal{M}^{(\pm)}$. This deviation varies between the sidebands which explains a large disparity of the corresponding angular profiles. When $\tau \approx T/2$, a minor deviation of the A and B parameters no longer essential, and their parametrization with Eq. (13) suffices. This way we arrive to the uniform SPA behavior exhibited in Fig. 3(c).

The SB14 is an exception from this rule. Its phase factor C_{14} is very different from other sidebands. First, it is less by about $\pi/2$ (or greater by $3\pi/2$) as seen in Fig. 5(c). The nature of this phase difference is explained in Ref. [18] in terms of the RABBITT phase transition across the ionization threshold. This transition also explains a very strong angular dependence at relatively small θ values where all other sidebands display essentially flat phase factors.

B. Mixed XUV harmonic spectrum

Laurent *et al.*[11] demonstrated that the RABBITT process can be strongly modified by adding even harmonics to the XUV spectrum. This modification follows from a newly opened single-photon ionization channel displayed in Fig. 6. Whereas the conventional RABBITT (a) is driven by two-path absorption and emission interference, the even harmonics-augmented XUV adds the third path (b). Accordingly, an additional term should be added to Eq. (11),

$$S_{2q}(\tau) = |\mathcal{M}_k + i\mathcal{M}_k^{(-)}e^{-i\omega\tau} + i\mathcal{M}_k^{(+)}e^{+i\omega\tau}|^2$$
$$\equiv A' + B\cos[2\omega\tau - C] + b\sin[\omega\tau - c], \quad (26)$$

where

$$A' = |\mathcal{M}_k|^2 + |\mathcal{M}_k^{(+)}|^2 + |\mathcal{M}_k^{(-)}|^2$$
$$> A = |\mathcal{M}_k^{(+)}|^2 + |\mathcal{M}_k^{(-)}|^2. \quad (27)$$

The b and c parameters can be expressed, respectively, via the magnitude and phase of the cross-product terms of the two-photon $\mathcal{M}_k^{(+)}$, $\mathcal{M}_k^{(-)}$ and one-photon $\mathcal{M}_k$ amplitudes (see the derivation in the Appendix). Unlike the conventional RABBITT, the sideband amplitude (26) acquires the ω oscillation due to the interference of the two-photon and single-photon processes exhibited in Figs. 6(a) and 6(b), respectively.

To generate a mixed harmonic XUV spectrum, we modify the individual pulselet phase Φ_n in the APT form (5). Whereas $\Phi_{2n\pm1} = 180°$ gives the purely odd harmonic spectrum, its slight reduction to $\Phi_{2n\pm1} = 170°$ generates the odd and even harmonic mix as shown in Fig. 7. In both cases, $\Phi_{2n} = 0$. One would expect that the photoelectron spectrum driven by, thus, modified APT will be similar with the XUV + IR driven spectrum shown in Fig. 1(k) and the contribution of the (a) and (b) processes illustrated in Fig. 6 will be comparable.

Whereas the alteration of the XUV spectrum shown in Fig. 7 seems to be miniscule, the corresponding modification of the photoelectron momentum distribution is drastic. In Fig. 8, we display the PMD projected on the $p_y = 0$ plane for the sidebands SB14–20 originated from the $2p_m$ initial state with (a) $m = 0$ and (b) $m = 1$. The time delay between the XUV and the IR pulses is set to zero. The analogous PMD's generated with the odd harmonics only APT are displayed in Figs. 1(d) and 1(e), respectively. Comparison of the corresponding distributions reveals a radical transformation of the PMD symmetry. Whereas the odd harmonics XUV generate the sidebands of the distinct Y_{3m} symmetry, a minimal mix of the even harmonics turn this symmetry into Y_{2m}. This
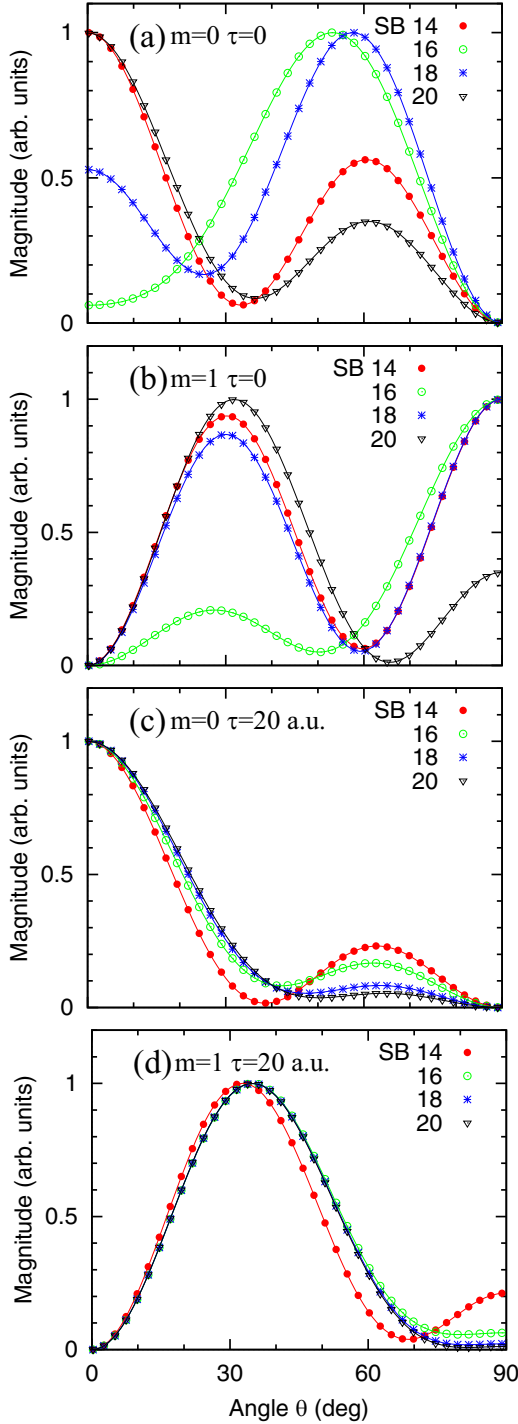
FIG. 2. Angular profiles of the sidebands SB14–20. The initial $2p_m$ state is prepared with $m = 0$ in (a) and (c) and $m = 1$ in (b) and (d). The XUV-IR delay $\tau = 0$ in (a) and (b) and $\tau = 20$ a.u. in (c) and (d). The raw data are displayed with the points. The similarly colored solid lines visualize the analytic fit with Eq. (23).

change in symmetry is most obvious in the $p_z = 0$ direction corresponding to $\theta = 90°$.

This symmetry change can be understood from the parametrization of Eq. (26). In Fig. 9, we plot the A', b, c parameters entering Eq. (26) as functions of the photoelectron ejection angle θ. The remaining parameters B, C hardly
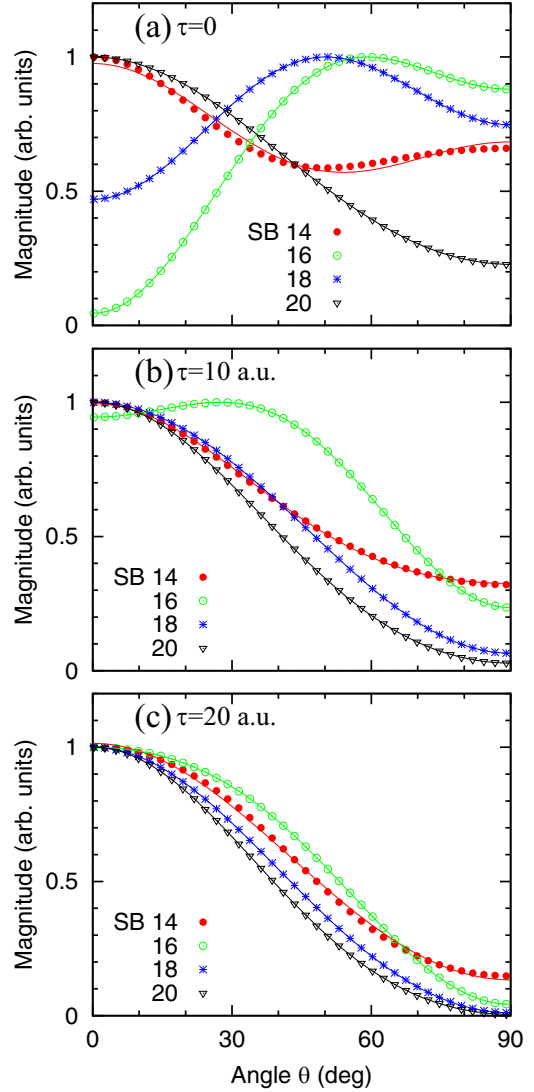
FIG. 3. Angular profiles of the sidebands SB14–20 summed over the angular momentum projections $\Sigma m = 0, \pm 1$. The XUV-IR time delay (a) $\tau = 0$, (b) 10 a.u., and (c) 20 a.u. The raw data are plotted with the points. The β parametrization by Eq. (14) is displayed with the similarly colored solid lines.

change with the XUV spectrum modification. By comparing the A and A' parameters displayed in the top panels of Figs. 5 and 9, respectively, we observe a strong increase $A' > A$ as prescribed by Eq. (26). At $\tau = 0$,

$$S_{2q}(\tau) \simeq A' - B \simeq A' - A = |\mathcal{M}_k|^2. \qquad (28)$$

Here we used $A \simeq B$ and $c \simeq 0$ for the most of its angular range except SB14. Thus, we see that at $\tau = 0$, the sidebands are driven entirely by the single photon ionization amplitudes. The photoelectron continuum is strongly dominated by the d wave according to the Fano propensity rule. Hence, the manifest display of the Y_{2m} angular symmetry.

IV. CONCLUDING REMARKS

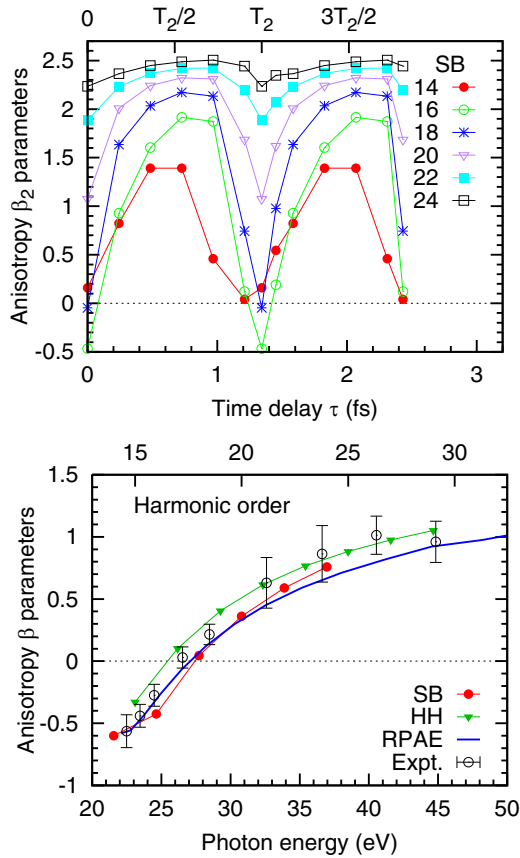In the present paper, we studied the photoelectron momentum distribution in the two-photon XUV-IR ionization of

FIG. 4. Top: the angular anisotropy β_2 parameter deduced from the fit with Eq. (14) as a function of the XUV-IR delay τ for various sidebands. The fractions of the period of the RABBITT oscillation $T_2 = \pi/\omega$ are marked at the top horizontal axis. Bottom: the angular anisotropy β parameter expressed via β_2 at $\tau = T_2/2$ a.u. for various SBs. Also shown are the corresponding values derived from primary harmonic peaks (HH) using Eq. (17) and calculated in the random-phase approximation with exchange (RPAE) [9]. The experimental data are from Ref. [26].

FIG. 5. The A, B, C parameters entering Eq. (1) as functions of the photoelectron ejection angle θ. The raw data points are joined with the similarly colored solid lines which visualize the analytic fit with Eq. (24).

the Ne atom. We projected this momentum distribution on the plane containing the joint polarization axis of the linearly polarized XUV and IR laser pulses. We identified the main features in the photoelectron spectrum in the form of the prime harmonic peaks associated with the XUV photon absorption and the IR-aided sidebands. Projections of the both sets of the spectral features display very clear angular symmetry associated with the respective set of spherical harmonics. This symmetry allows us to identify the partial-wave composition of the photoelectron continuum resulted from the XUV and XUV + IR photon absorption. Whereas the XUV-only continuum adheres to the Fano propensity rule [17], the angular composition of the XUV + IR continuum is more complex and does not always support a simple extension of the Fano rule to continuous-continuous transitions suggested in Ref. [7].

We also explain the evolution of the SB angular profiles with increasing XUV-IR delay τ. At zero delay, the angular profiles display a very diverse behavior between various sidebands. When τ approaches half a period of the RABBITT oscillation $T_2/2$, this behavior becomes universal across all
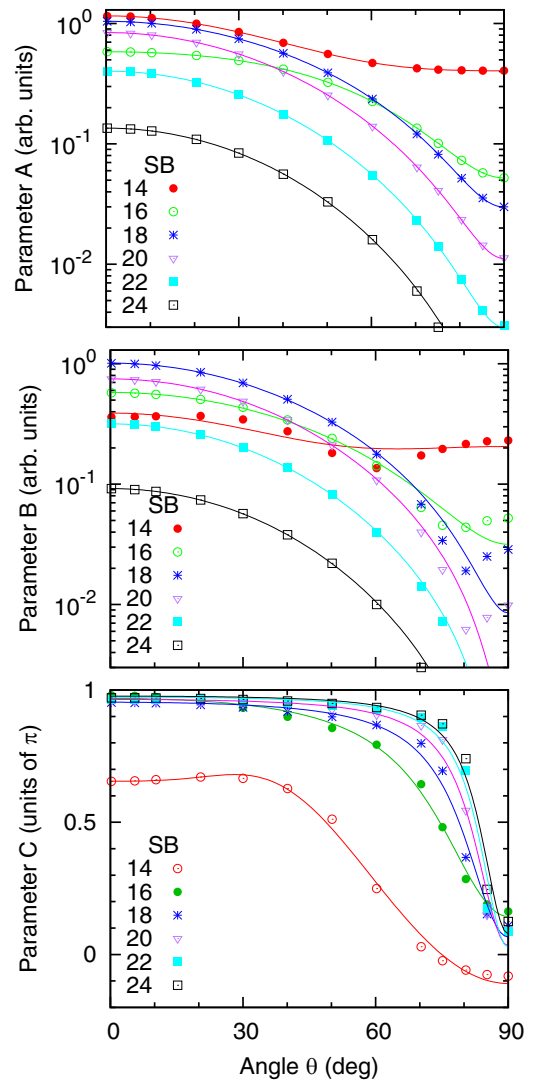
the sidebands as required by the soft photon regime of the IR absorption and emission. The SB14 breaks away from this rule because of the RABBITT-uRABBITT phase transition. The onset of the SPA at half periods of the RABBITT oscillations explains the convergence of the β_2 angular anisotropy parameters across various sidebands. This effect was observed earlier in Ar [7], but it did not receive a qualitative explanation.

The present paper can be expanded to other atomic targets. The uRABBITT behavior is universal. So far, it has been demonstrated in Ne [15,16] and He [14]. Other atoms can be accessed with an appropriate choice of the driving laser pulse parameters. Utility of uRABBITT as a novel spectroscopic technique has been demonstrated in Ref. [19] by making a detailed mapping of the bound states energies and oscillator strengths in Ne. Following the preceding works [15,16], the present paper broadens the use of the angular-resolved uRABBITT technique which allows bringing an additional wealth of useful information. We hope that our results will
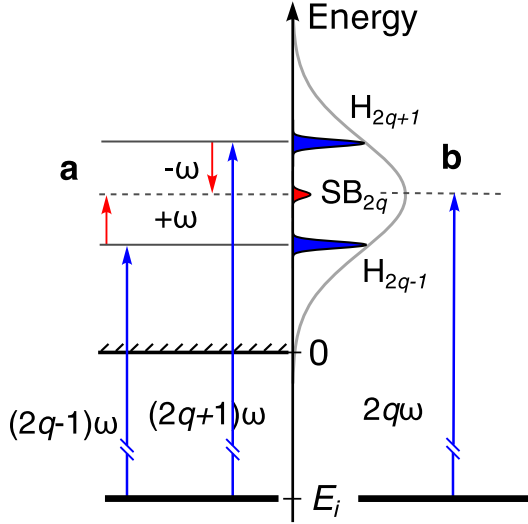
FIG. 6. (a) Schematic of the RABBITT process driven by odd harmonics in the XUV spectrum $(2n \pm 1)\omega$. (b) An additional channel which opens by adding even harmonics $2n\omega$ to the APT.

stimulate further uRABBITT experiments. Some preliminary results have already been presented [27].

Finally, we have considered an APT comb with both the odd and the even harmonic orders. Such a comb can be produced from high-order harmonic generation sources driven by the fundamental frequency and its second harmonic [11,15]. The angular momentum composition and the β expansion become significantly more complex and reveal a greater diversity of various physical effects. In addition, the ω oscillation becomes present in the RABBITT signal, thus, changing the time and angular momentum structure of the photoelectron continuum.
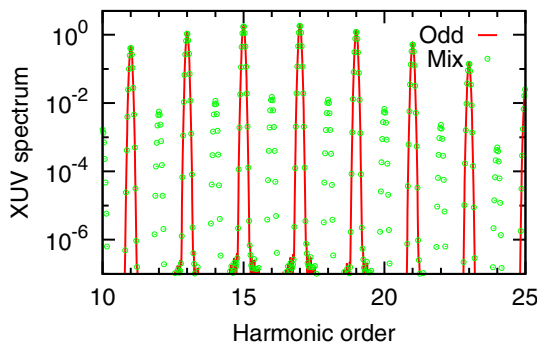
FIG. 7. XUV field spectrum generated with the pulselett phase factor $\Phi_{2n\pm 1} = 180°$ (odd harmonics) and (mixed harmonics). $\Phi_{2n\pm 1} = 170°$.
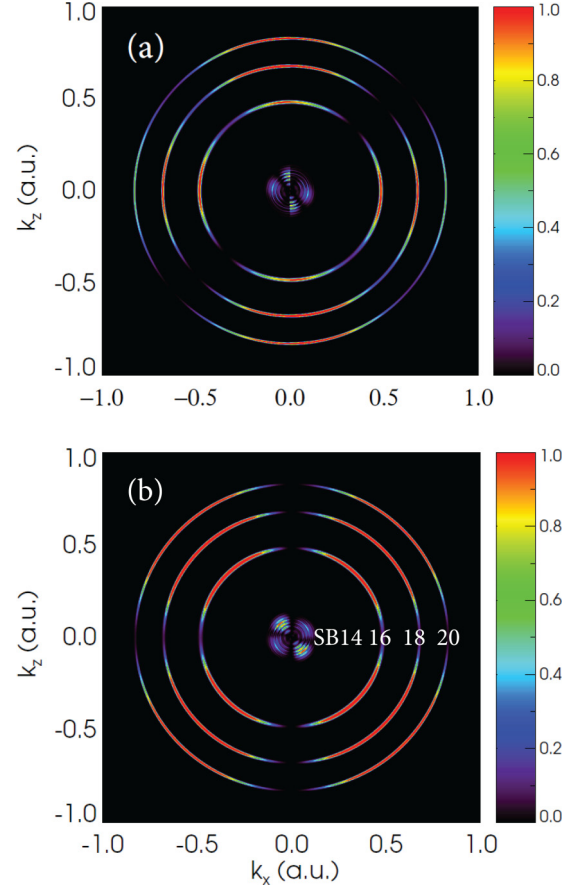

FIG. 8. The PMD originated from the $2p_m$ initial state of Ne projected on the $p_y = 0$ plane. The sidebands SB14–20 are visualized with (a) $m = 0$ and (b) $m = 1$. The time delay between the XUV and IR $\tau = 0$.

APPENDIX: MIXED PARITY RABBITT INTERFERENCE

The mixed parity RABBITT amplitude contains the first- and second-order interference (FSI) term [11],

$$S_{2q}(\tau)$$
$$= |\mathcal{M}_k + i\mathcal{M}_k^{(-)}e^{-i\omega\tau} + i\mathcal{M}_k^{(+)}e^{+i\omega\tau}|^2$$
$$= |\mathcal{M}_k|^2 + |\mathcal{M}_k^{(-)}|^2 + |\mathcal{M}_k^{(+)}|^2, \quad \text{DC term}$$
$$+ 2\text{Re}[\mathcal{M}_k^{(-)}\mathcal{M}_k^{*(+)}e^{i\pi}e^{-2i\omega\tau}], \quad \text{RABBITT term}$$
$$+ 2\text{Re}[i\mathcal{M}_k\mathcal{M}_k^{*(+)}e^{-i\omega\tau} + i\mathcal{M}_k^*\mathcal{M}_k^{(-)}e^{-i\omega\tau}], \quad \text{FSI term}$$
$$\equiv A' + B\cos[2\omega\tau - C] + b\sin[\omega\tau - c]. \quad (A1)$$

In transforming the RABBITT term, we note that

$$2\text{Re}[\mathcal{M}_k^{(-)}\mathcal{M}_k^{*(+)}e^{i\pi}e^{-2i\omega\tau}] =$$
$$= 2|\mathcal{M}_k^{(-)}\mathcal{M}_k^{(+)}|\text{Re}\exp\{i\arg[\mathcal{M}_k^{(-)}\mathcal{M}_k^{*(+)}] + \pi - 2i\omega\tau\}$$
$$= 2|\mathcal{M}_k^{(-)}\mathcal{M}_k^{(+)}|\cos(2\omega\tau - \pi - \arg[\mathcal{M}_k^{(-)}\mathcal{M}_k^{*(+)}])$$
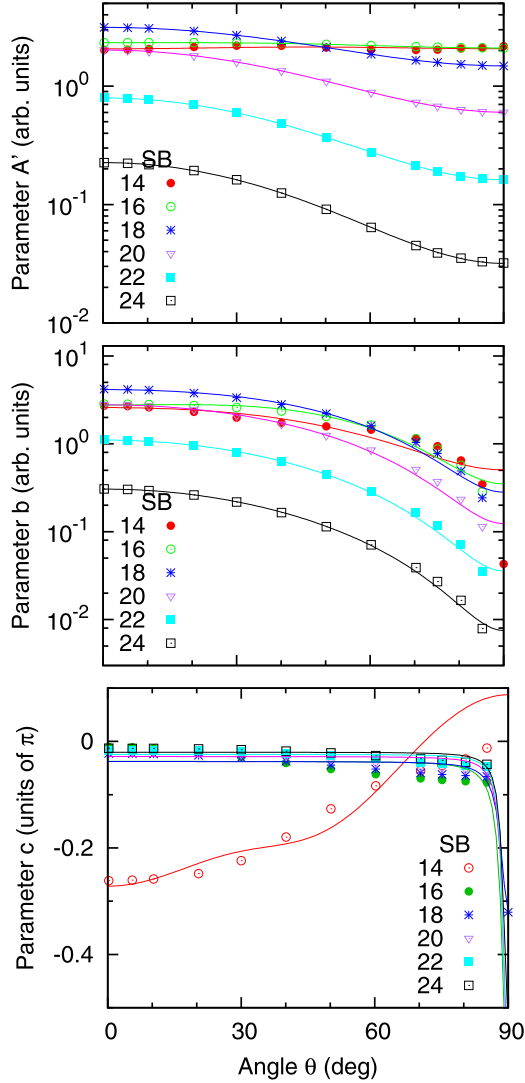$$\equiv \cos(2\omega\tau - C), \quad C = \pi + \arg[\mathcal{M}_k^{(-)}\mathcal{M}_k^{*(+)}]. \quad (A2)$$

FIG. 9. The A', b, c parameters entering Eq. (26) as functions of the photoelectron ejection angle θ. The raw data points are joined with the similarly colored solid lines which visualize the analytic fit with Legendre polynomials.

Similarly,

$$2\,\mathrm{Re}[i\mathcal{M}_k \mathcal{M}_k^{*(+)} e^{-i\omega\tau} + i\mathcal{M}_k^* \mathcal{M}_k^{(-)} e^{-i\omega\tau}] =$$

$$-2\mathrm{Im}[\mathcal{M}_k \mathcal{M}_k^{*(+)} e^{-i\omega\tau} + \mathcal{M}_k^* \mathcal{M}_k^{(-)} e^{-i\omega\tau}] = b\,\sin[\omega\tau - c]$$

$$-2|\mathcal{M}_k \mathcal{M}_k^{*(+)} + \mathcal{M}_k^* \mathcal{M}_k^{(-)}| = b$$

$$\arg[\mathcal{M}_k \mathcal{M}_k^{*(+)} + \mathcal{M}_k^* \mathcal{M}_k^{(-)}] = c. \qquad \text{(A3)}$$

To estimate the FSI phase c in Eq. (A3), we assume a weak absorption and emission asymmetry $\mathcal{M}_k^{(+)} \simeq \mathcal{M}_k^{(-)}$. We define the mixed amplitude products,

$$\mathcal{M}_k \mathcal{M}_k^{*(+)} = P, \qquad \mathcal{M}_k \mathcal{M}_k^{*(-)} = M.$$

The expression of our interest,

$$\arg[P + M^*] = \arg\left[1 + \frac{M^* - P^*}{P + P^*}\right]$$

$$\approx \mathrm{Im}\frac{M^* - P^*}{P + P^*} = \frac{\mathrm{Im}[\mathcal{M}_k^* \mathcal{M}_k^{(-)} - \mathcal{M}_k^* \mathcal{M}_k^{(+)}]}{2\,\mathrm{Re}\,\mathcal{M}_k^* \mathcal{M}_k^{(+)}}$$

$$\approx \approx \frac{\mathrm{Im}[\mathcal{M}_k^{(-)} - \mathcal{M}_k^{(+)}]}{2\,\mathrm{Re}\,\mathcal{M}_k^{(+)}} \quad \text{if } \mathcal{M}_k \text{ is real.} \quad \text{(A4)}$$

Here we used $\arg(1 + z) \approx \mathrm{Im}\,z$ if $|z| \ll 1$. Furthermore,

$$\frac{\mathrm{Im}[\mathcal{M}_k^{(-)} - \mathcal{M}_k^{(+)}]}{2\,\mathrm{Re}\,\mathcal{M}_k^{(+)}} = \frac{|\mathcal{M}_k^{(-)}|\sin\phi^{(-)} - |\mathcal{M}_k^{(+)}|\sin\phi^{(+)}}{2|\mathcal{M}_k^{(+)}|\cos\phi^{(+)}}$$

$$\approx \frac{\sin\phi^{(-)} - \sin\phi^{(+)}}{2\cos\phi^{(+)}}$$

$$= \frac{2\cos\frac{1}{2}[\phi^{(-)} + \phi^{(+)}]\sin\frac{1}{2}[\phi^{(-)} - \phi^{(+)}]}{2\cos\phi^{(+)}}$$

$$\approx \frac{1}{2}[\phi^{(-)} - \phi^{(+)}] = \arg[\mathcal{M}_k^{(-)} \mathcal{M}_k^{*(+)}]. \quad \text{(A5)}$$

By comparing Eqs. (A5) and (A3), we connect the phases of the RABBITT 2ω and ω oscillations,

$$C - \pi = 2c. \qquad \text{(A6)}$$

Our numerical values derived from the TDSE solution driven by a mixed harmonics APT satisfy this identity to a high precision.

[1] M. Schultze, M. Fiess, N. Karpowicz, J. Gagnon, M. Korbman, M. Hofstetter, S. Neppl, A. L. Cavalieri, Y. Komninos, T. Mercouris *et al.*, Delay in photoemission, Science **328**, 1658 (2010).

[2] P. M. Paul, E. S. Toma, P. Breger, G. Mullot, F. Augé, P. Balcou, H. G. Muller, and P. Agostini, Observation of a train of attosecond pulses from high harmonic generation, Science **292**, 1689 (2001).

[3] Y. Mairesse, A. de Bohan, L. J. Frasinski, H. Merdji, L. C. Dinu, P. Monchicourt, P. Breger, M. Kovacev, R. Taïeb, B. Carré *et al.*, Attosecond synchronization of high-harmonic soft x-rays, Science **302**, 1540 (2003).

[4] K. Klünder, J. M. Dahlström, M. Gisselbrecht, T. Fordell, M. Swoboda, D. Guénot, P. Johnsson, J. Caillat, J. Mauritsson, A. Maquet, R. Taieb, and A. L'Huillier, Probing Single-Photon Ionization on the Attosecond Time Scale, Phys. Rev. Lett. **106**, 143002 (2011).

[5] S. Heuser, A. Jiménez Galán, C. Cirelli, C. Marante, M. Sabbar, R. Boge, M. Lucchini, L. Gallmann, I. Ivanov, A. S. Kheifets, J. M. Dahlström, E. Lindroth, L. Argenti, F. Martín, and U. Keller, Angular dependence of photoemission time delay in helium, Phys. Rev. A **94**, 063409 (2016).

[6] C. Cirelli, C. Marante, S. Heuser, C. L. M. Petersson, A. J. Galán, L. Argenti, S. Zhong, D. Busto, M. Isinger, S. Nandi *et al.*, Anisotropic photoemission time delays close to a Fano resonance, Nat. Commun. **9**, 955 (2018).

[7] D. Busto, J. Vinbladh, S. Zhong, M. Isinger, S. Nandi, S. Maclot, P. Johnsson, M. Gisselbrecht, A. L'Huillier, E. Lindroth, and J. M. Dahlström, Fano's Propensity Rule in Angle-Resolved Attosecond Pump-Probe Photoionization, Phys. Rev. Lett. **123**, 133201 (2019).

[8] I. A. Ivanov and A. S. Kheifets, Angle-dependent time delay in two-color XUV+IR photoemission of He and Ne, Phys. Rev. A **96**, 013408 (2017).

[9] A. W. Bray, F. Naseem, and A. S. Kheifets, Simulation of angular-resolved RABBITT measurements in noble-gas atoms, Phys. Rev. A **97**, 063404 (2018).

[10] J. M. Dahlström, D. Guénot, K. Klünder, M. Gisselbrecht, J. Mauritsson, A. L'Huillier, A. Maquet, and R. Taïeb, Theory of attosecond delays in laser-assisted photoionization, Chem. Phys. **414**, 53 (2013).

[11] G. Laurent, W. Cao, H. Li, Z. Wang, I. Ben-Itzhak, and C. L. Cocke, Attosecond Control of Orbital Parity Mix Interferences and the Relative Phase of Even and Odd Harmonics in an Attosecond Pulse Train, Phys. Rev. Lett. **109**, 083001 (2012).

[12] A. Maquet and R. Taïeb, Two-colour IR+XUV spectroscopies: the soft-photon approximation, J. Mod. Opt. **54**, 1847 (2007).

[13] S. Southworth, A. Parr, J. Hardis, J. Dehmer, and D. Holland, Calibration of a monochromator/spectrometer system for the measurement of photoelectron angular distributions and branching ratios, Nucl. Instrum. Methods Phys. Res., Sect. A **246**, 782 (1986).

[14] M. Swoboda, T. Fordell, K. Klünder, J. M. Dahlström, M. Miranda, C. Buth, K. J. Schafer, J. Mauritsson, A. L'Huillier, and M. Gisselbrecht, Phase Measurement of Resonant Two-Photon Ionization in Helium, Phys. Rev. Lett. **104**, 103003 (2010).

[15] D. M. Villeneuve, P. Hockett, M. J. J. Vrakking, and H. Niikura, Coherent imaging of an attosecond electron wave packet, Science **356**, 1150 (2017).

[16] S. Patchkovskii, M. J. J. Vrakking, D. M. Villeneuve, and H. Niikura, Selection of the magnetic quantum number in resonant ionization of neon using an XUV–IR two-color laser field, J. Phys. B: At. Mol. Opt. Phys. **53**, 134002 (2020).

[17] U. Fano, Propensity rules: An analytical approach, Phys. Rev. A **32**, 617 (1985).

[18] A. S. Kheifets and A. W. Bray, RABBITT phase transition across the ionization threshold, Phys. Rev. A **103**, L011101 (2021).

[19] A. Kheifets, Revealing the target electronic structure with under-threshold RABBITT, Atoms **9**, 66 (2021).

[20] G. Wendin and A. F. Starace, Perturbation theory in a strong-interaction regime with application to 4d-subshell spectra of ba and la, J. Phys. B: At. Mol. Phys. **11**, 4119 (1978).

[21] A. Kramida, Y. Ralchenko, J. Reader, and NIST ASD Team, NIST Atomic Spectra Database (ver. 5.2), [Online]. Available: http://physics.nist.gov/asd [2015, June 30]. National Institute of Standards and Technology, Gaithersburg, MD (2014).

[22] S. Patchkovskii and H. Muller, Simple, accurate, and efficient implementation of 1-electron atomic time-dependent schrödinger equation in spherical coordinates, Comput. Phys. Commun. **199**, 153 (2016).

[23] L. Tao and A. Scrinzi, Photo-electron momentum spectra from minimal volumes: the time-dependent surface flux method, New J. Phys. **14**, 013021 (2012).

[24] F. Morales, T. Bredtmann, and S. Patchkovskii, iSURF: a family of infinite-time surface flux methods, J. Phys. B: At. Mol. Opt. Phys. **49**, 245001 (2016).

[25] V. Véniard, R. Taïeb, and A. Maquet, Phase dependence of $(n+1)$-color $(n>1)$ ir-uv photoionization of atoms with higher harmonics, Phys. Rev. A **54**, 721 (1996).

[26] K. Codling, R. G. Houlgate, J. B. West, and P. R. Woodruff, Angular distribution and photoionization measurements on the 2p and 2s electrons in neon, J. Phys. B: At. Mol. Phys. **9**, L83 (1976).

[27] M. Moioli, K. R. Hamilton, H. Ahmadi, D. Ertel, M. Schmoll, M. M. Popova, E. V. Gryzlova, A. N. Grum-Grzhimailo, M. D. Kiselev, D. Atri-Schuller *et al.*, Attosecond time delays near the photoionisation threshold of neon, Photonic, Electronic, and Atomic Collisions (32 vICPEAC) p. J31 (2021).